Applied Physics Letters

RESEARCH ARTICLE | JUNE 26 2024

Tunable spike-timing-dependent plasticity in magnetic skyrmion manipulation chambers

Zulfidin Khodzhaev ; Jean Anne C. Incorvia

Check for updates

Appl. Phys. Lett. 124, 262402 (2024)
https://doi.org/10.1063/5.0218348

View Online
Export Citation

26 June 2024 14:52:50

Applied Physics Letters
Special Topic:
Quantum Networks
Guest Editors: David Awschalom, Ronald Hanson, Stephanie Simmons
Submit Today!
AIP Publishing

AIP Publishing

Applied Physics Letters ARTICLE pubs.aip.org/aip/apl

Tunable spike-timing-dependent plasticity in magnetic skyrmion manipulation chambers

Cite as: Appl. Phys. Lett. **124**, 262402 (2024); doi: 10.1063/5.0218348
Submitted: 10 May 2024 · Accepted: 17 June 2024 ·
Published Online: 26 June 2024

View Online Export Citation CrossMark

Zulfidin Khodzhaev and Jean Anne C. Incorvia[a)]

AFFILIATIONS

Chandra Family Department of Electrical and Computer Engineering, The University of Texas at Austin, Austin, Texas 78712, USA

[a)]Author to whom correspondence should be addressed: incorvia@austin.utexas.edu

ABSTRACT

Magnetic skyrmions, as scalable and nonvolatile spin textures, can dynamically interact with fields and currents, making them promising for unconventional computing. This paper presents a neuromorphic device based on skyrmion manipulation chambers to implement spike-timing-dependent plasticity (STDP), a mechanism for unsupervised learning in brain-inspired computing. STDP adjusts synaptic weights based on the timing of pre-synaptic and post-synaptic spikes. The proposed three-chamber design encodes synaptic weight in the number of skyrmions in the center chamber, with left and right chambers for pre- and post-synaptic spikes, respectively. Micromagnetic simulations demonstrate that the timing between applied currents across the chambers controls the final skyrmion count (weight). The device exhibits adaptability and learning capabilities by manipulating chamber parameters, mimicking Hebbian and dendritic location-based plasticity. The device's ability to maintain state post-write highlights its potential for advancing adaptable neuromorphic devices.

Published under an exclusive license by AIP Publishing. https://doi.org/10.1063/5.0218348

26 June 2024 14:52:50

Emulating neural brain functions in solid-state devices is a central focus in neuromorphic computing due to its potential for energy-efficient computing.[1,2] Neuromorphic systems aim to mimic the highly parallel, event-driven, and adaptive nature of biological neural networks.[3–5] Spike-timing-dependent plasticity (STDP), which adjusts synaptic weight based on the timing of pre- and post-synaptic spikes,[6,7] is fundamental to unsupervised learning in the brain, where synapses independently optimize for learning and memory recall.[8] STDP has been extensively studied in biological systems and has been shown to play a crucial role in the development and refinement of neural circuits.[9,10] Fine-tuning the time constant and amplitude of synaptic weight changes is crucial in this process, as it allows the network to adapt the speed and magnitude of synaptic changes to specific computational tasks or environmental conditions. The adaptability of spiking neural networks (SNNs), similar to biological synapses, enhances their learning capabilities, responsiveness, and overall efficiency, proving helpful in managing complex dynamics over extended periods and training neural networks with long-term temporal dependencies.[11–13] Recent advances in hardware implementation of SNNs have demonstrated their potential for energy-efficient and fast information processing.[14,15] Magnetic skyrmions, small magnetic textures found in certain magnetic materials, are attracting attention due to their unique properties[16] with application in computing, particularly their dynamics in confined geometries,[17,18] and their potential use as artificial synapses in neuromorphic computing.[19]

Previous studies have investigated the behavior of magnetic skyrmions in manipulation chambers and under the influence of temperature,[17,18,20] including the design and examination of a skyrmion manipulation chamber for stochastic computing.[18] These studies have shown that skyrmions can be efficiently controlled and manipulated using electrical currents and temperature gradients.[21–23] Moreover, magnetic skyrmions in a magnetic tunnel junction (MTJ) have been shown to act as artificial synapses,[19] exhibiting synaptic characteristics such as long-term potentiation (LTP) and long-term depression (LTD).[24–27] However, STDP has not been implemented in multi-skyrmion chamber devices that could be tuned to emulate various forms of synaptic plasticity.

Here, nanodevices based on magnetic skyrmion manipulation chambers are designed to implement STDP. The device is divided into distinct regions, each capable of applying different magnitudes and directions of current. Micromagnetic simulations analyze the device's behavior, demonstrating three different rates of STDP plasticity weight updates and several maximum weight updates. The simulations reveal that the skyrmions' dynamics under various current densities impact the rate of weight updates. This research develops adaptable neuromorphic devices capable of mimicking different types of synaptic plasticity, e.g., Hebbian[6,9] and dendritic location-based plasticity.[9]

The STDP model is defined by a function $W(\Delta t)$, where Δt represents the difference in timing between pre- and post-synaptic spikes. The model has different forms depending on the order of neuron spikes,[28]

Published under an exclusive license by AIP Publishing

$$W(\Delta t) = \begin{cases} A^+ e^{-\Delta t/\tau^+}, & \Delta t \geq 0, \\ -A^- e^{\Delta t/\tau^-}, & \Delta t < 0, \end{cases}$$

where τ^+ (τ^-) are the time constants for potentiation (depression) that determine the strength of the update over a given interspike interval, A^+ and A^- represent the maximum and minimum synaptic changes, respectively, and $\Delta t = t_{post} - t_{pre}$ represents the time difference between the pre- and post-synaptic spikes.

The design of the device, composed of three chambers, is depicted in Fig. 1(a): two small chambers for the pre-synaptic spike chamber (Pre) and post-synaptic spike chamber (Post), and a middle weights chamber (W) for weight storage. In the proposed device, the synapse weight corresponds to the number of skyrmions in the W chamber after a spiking event and can be readout using an MTJ,[29] which measures the quantized change in resistance proportional to the total topological degree in the chamber. For the Pre and Post chambers, events are timed based on the current density and geometry, as the skyrmion dynamics in such confined geometries have been previously studied.[18,20] Each chamber has a controllable current density magnitude and direction, managed using contacts I_1, I_2, I_3, and I_4 and grounds between the middle and small chambers. Two voltage-controlled magnetic anisotropy (VCMA) gates are positioned between the spike and weights chambers, regulated by contacts V_1 and V_2.

The simulation is executed using MuMax3,[30] and the material parameters shown in Table I represent Ir/Co/Pt non-symmetric multilayers.[31] The simulation applies spin-transfer torque (STT) using the Zhang–Li model, with the spin polarization parameter set to 0.4 and the non-adiabaticity of STT set to 0.2.

In this study, the term "spike" functions as a self-regulating mechanism similar to the action potential in a biological neuron. The accumulation of skyrmions in the Pre or Post chamber is akin to the electrical potential buildup in a neuron. Once this count reaches 15 skyrmions, the maximum Pre and Post are designed to accumulate before skyrmions start leaving the chamber if gates are turned off—a spike is triggered, paralleling a neuron's action potential. This event marks a peak in system activity and causes a reset by turning off applied currents, stopping further skyrmion accumulation. Thus, it serves to regulate system activity and prevent potential overload.

TABLE I. Material parameters used in the simulation.

Symbol	Magnetic constant	Values
α	Gilbert damping	0.14
M_s	Saturation magnetization	9.6×10^5 A/m
K_u	Anisotropy constant	7.17×10^5 J/m^3
A	Exchange stiffness	1.6×10^{-11} J/m
DMI	Dzyaloshinskii–Moriya interaction	1.51×10^{-3} J/m^2

The initial magnetization is uniformly set out of plane ($\hat{z}$) as illustrated in Fig. 1(b), and a Néel skyrmion with charge 1 and core polarization -1 was introduced, shifted 1740 nm in the $\pm\hat{y}$ direction from the center of the geometry to the rectangular paths. The dimensions of the Pre and Post are 940 and 500 nm along the major and minor axis directions, respectively. The W measures 1250 and 900 nm in the $\hat{y}$ and $\hat{x}$ directions, respectively. A rectangle of width 210 nm connects the chambers. The rectangles extending from the left side of the "Pre" chamber and the right side of the "Post" chamber have a width of 180 nm. The spike chambers have been designed in an elliptical shape to accommodate more stable skyrmions. This results in a smoothed edge between the chamber and rectangle regions, preventing edge crashes involving skyrmions.[20] A 5 nm wide strip with a higher anisotropy constant (K_u) of 9.27×10^5 J/m^3 covers Pre and Post borders (Fig. 2) to repel skyrmions[32] and improves stability at elevated temperatures. Reference 20 provides a more detailed examination of temperature influence on manipulation chambers. To expedite the simulations, a damping constant $\alpha = 0.14$ was used, and the simulations were conducted at a temperature of 0 K. The discretization cell is set to $4 \times 4 \times 1$ nm^3 in the $\hat{x}$, $\hat{y}$, and $\hat{z}$ directions, respectively.

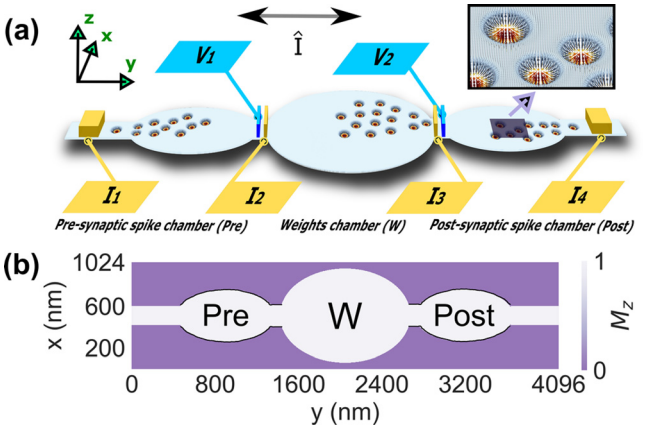

FIG. 1. STDP skyrmion chamber design and simulation setup. (a) The device consists of three chambers (two for spikes and one for weight update) controlled by four contacts (I_1–I_4) applying current in $\pm\hat{y}$ directions. VCMA contacts (V_1, V_2) prevent skyrmion overflow. An inset displays simulated skyrmion snapshots. (b) Simulation setup includes initial magnetization and geometric dimensions, with a 5 nm wide strip ($K_u = 9.27 \times 10^5$ J/m^3) surrounding Pre and Post regions.

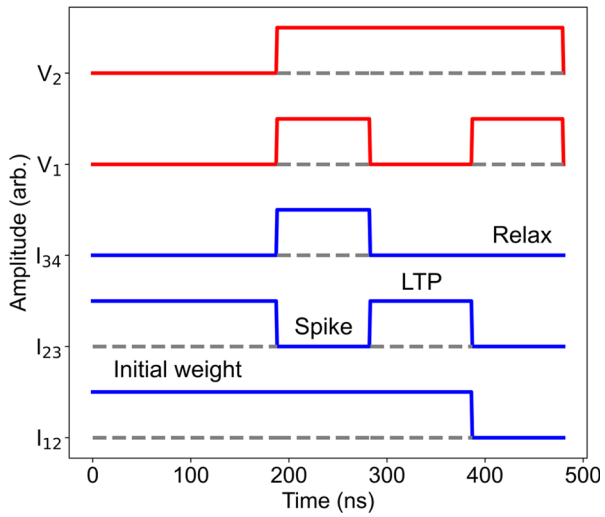

FIG. 2. Sequence and timing of currents (I_{12}, I_{23}, I_{34}), voltages (V_1, V_2), and key operations (initial weight, spike on the left/right, LTP, and system relaxation) in the skyrmion chamber device during the long-term potentiation process.

26 June 2024 14:52:50

Published under an exclusive license by AIP Publishing

Table II outlines the range of functions the STDP skyrmion chamber can be tailored to perform, and Fig. 2 shows its timing diagram for the long-term potentiation (LTP) process. The system starts operations with an initial number of skyrmions (initial weight) in the center chamber, which can be introduced via either Pre or Post. In this study, the initial weight was introduced via Pre using I_{12} and I_{23}. Next, skyrmions accumulate in Pre and Post using I_{12} and I_{34} currents, while V_1 and V_2 keep skyrmions moving to the W. When the skyrmion count in either chamber reaches a predetermined threshold of 15, V_1 is turned off to let skyrmions pass, i.e., the neuron spikes. The VCMA gates increase the anisotropy constant, creating high energy barriers that lead to the annihilation of the skyrmions. The temporal difference between the spikes activates the respective currents for LTP (I_{12}, I_{23}), and meanwhile, V_2 is kept active to prevent overflow from W to Post. The current is applied in the $-\hat{y}$ direction. After the LTP process, the system enters a relaxation stage, where currents are turned off and VCMA gates are kept on until the next spike event is observed.

Following these events, the system undergoes a relaxation phase lasting 100 ns, during which skyrmion–skyrmion repulsion comes into play, increasing the area covered by skyrmions. This demonstrates the device's non-volatility to retain its state post-write. The VCMA gates are simulated using higher anisotropy constant of $K_u = 9.27 \times 10^5$ J/m^3 when the gate is on, and $K_u = 7.17 \times 10^5$ J/m^3 when the gate is off, returning to the intrinsic anisotropy constant of the material.

Figure 2 shows the interplay of currents (I_{12}, I_{23}, I_{34}) and voltages (V_1, V_2) for the LTP synaptic plasticity function when $\Delta t = 0$, as described in Table II. Details of the process are animated in the supplementary material video S1.

Figure 3 shows simulation snapshots and results that illustrate the initial weight transfer and the effect of spike-timing delays on the weight update. Figures 3(a)–3(f) plot the initial weight transfer from Pre to W with magnetization snapshots at t = 30 (a), 94 (b), and 186 ns (c). The arrow indicates the direction of the skyrmion propagation. Figure 3(d) shows the corresponding skyrmion number in the Pre, (e) shows for the W chamber, and (f) shows the Post chamber. For initial weight, $I_{12} = 4.5 \times 10^{11}$ A/m^2 $(-\hat{y})$ and $I_{23} = 2.5 \times 10^{11}$ A/m^2 $(-\hat{y})$ were applied. The ground is connected to both the region between the Pre and W chambers and the region between the Post and W chambers to allow independently supplied currents.

Previous experimental[17] and theoretical[20] work demonstrated that current density was lower in the chamber section of the skyrmion reshuffle device compared to the rectangular sections due to its larger size. This pattern was replicated in modeling the chambers by

TABLE II. Setup for various STDP skyrmion chamber device operations. For example, I_{12} column indicates the presence and direction of current flowing between electrodes I_1 and I_2.

I_{12}	I_{23}	I_{34}	V_1	V_2	Function
$-\hat{y}$	$-\hat{y}$	OFF	OFF	OFF	Initial weight
$-\hat{y}$	OFF	OFF	ON	ON	Spike on the left
OFF	OFF	$+\hat{y}$	ON	ON	Spike on the right
$-\hat{y}$	$-\hat{y}$	OFF	OFF	ON	Long-term potentiation
OFF	$-\hat{y}$	$-\hat{y}$	ON	OFF	Long-term depression
OFF	OFF	OFF	ON	ON	System relaxation

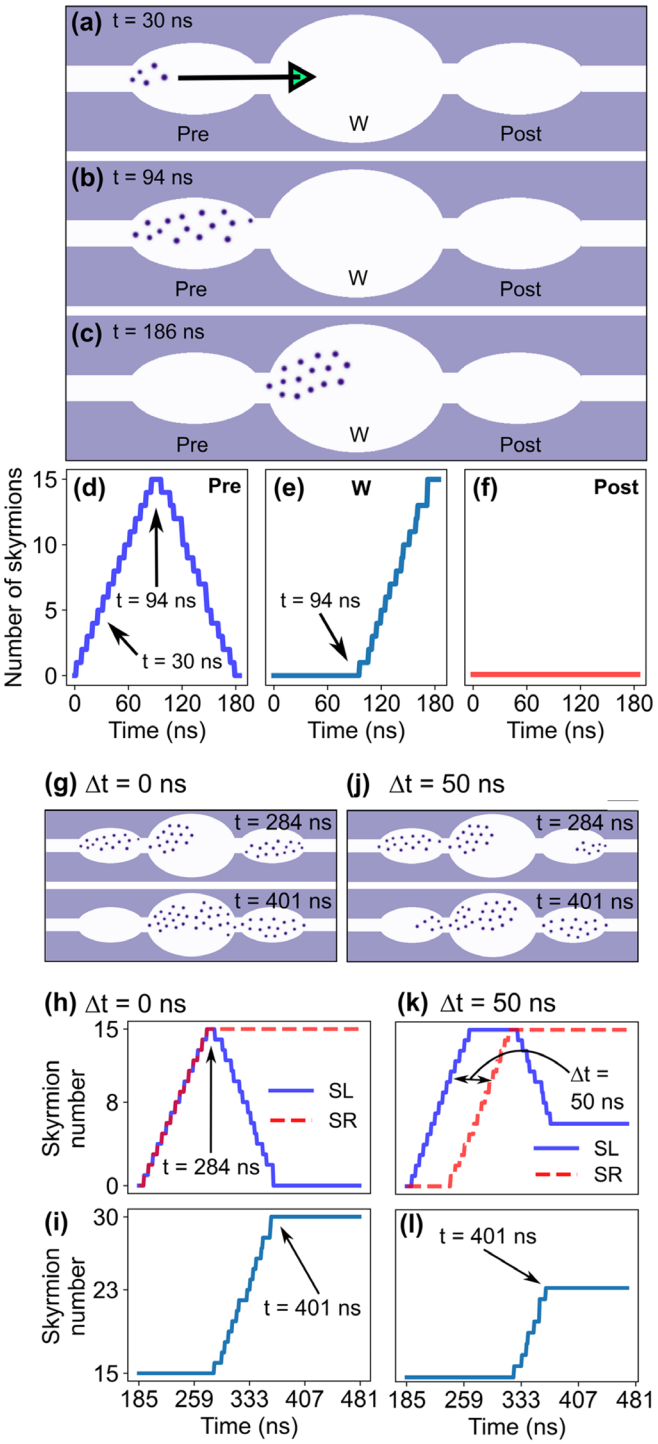

FIG. 3. Initial weight operation and comparative analysis of $\Delta t = 0$ and $\Delta t = 50$ ns spikes for LTP. (a)–(c) Magnetization simulation snapshots of Pre, W, and Post at 30, 94, and 186 ns, respectively. Arrow in (a) indicates skyrmion movement direction. (d)–(f) Weight updates in Pre, W, and Post. (g)–(i) Initial weight, skyrmion number over time, and weight update for $\Delta t = 0$. (j)–(l) Same for $\Delta t = 50$ ns between SL and SR.

26 June 2024 14:52:50

Published under an exclusive license by AIP Publishing

assigning a higher current density in the rectangles, e.g., the left rectangle of Pre (1.8×10^{12} A/m^2) and a lower density within the chamber (4.5×10^{11} A/m^2). The same pattern was used for the Post chamber. As a result, skyrmions move quickly toward the spiking chambers and then slow down, allowing time for interaction and accumulation. For the remainder of this paper, only the current density within the spiking chambers will be referred to for both I_{12} and I_{34} currents.

The DBSCAN algorithm[33] from Python's sklearn library was used to detect and count skyrmions in the Pre, W, and Post chambers. Figures 3(g)–3(l) show the effect of the delay between spike on the left chamber (SL) and spike on the right chamber (SR) on the weight update in W. When the delay is $\Delta t = 0$ ns [Figs. 5(g)–5(i)], both Pre and Post reach 15 skyrmions simultaneously at t = 284 ns, and the weight update is maximized, increasing from 15 to 30 skyrmions in W at t = 401 ns. With a 50 ns delay [Figs. 5(j)–5(l)], the weight increases from 15 to 23 skyrmions, resulting in a lower update. The delay corresponds to the I_{12} and I_{23} currents runtime. For all 15 skyrmions, the runtime to move from Pre to W is 100 ns; for each Δt, the runtime gets subtracted. VCMA remains active until either Pre or Post reaches the spike threshold. For SL and SR, $I_{12} = 4.5 \times 10^{11}$ A/m^2 $(-\hat{y})$ and $I_{34} = 4.5 \times 10^{11}$ A/m^2 $(+\hat{y})$ are used. For LTP, $I_{12} = 4.5 \times 10^{11}$ A/m^2 $(-\hat{y})$ and $I_{23} = 2.5 \times 10^{11}$ A/m^2 $(-\hat{y})$ are applied.

Figure 4 shows the LTP and LTD characteristics for different spike-timing delays (Δt) and STDP curves mimicking dendritic location-dependent plasticity. In LTP [Fig. 4(a)], the synaptic weight update inversely depends on Δt, with the range of changes varying from 0% (15 skyrmions) to 100% (30 skyrmions). The initial jump and drop are attributed to the activation of VCMA gates. In LTD [Fig. 4(b)], as $|\Delta t|$ increases, the net synaptic weight removed from W decreases, with maximum and minimum changes corresponding to 100% (0 skyrmions) and 0% (15 skyrmions). For LTD, $I_{23} = 3.5 \times 10^{11}$ A/m^2 $(-\hat{y})$ $(\Delta t > 0)$ and $I_{34} = 4.5 \times 10^{11}$ A/m^2 $(-\hat{y})$ $(\Delta t < 0)$ are applied. The total runtime is kept at 100 ns by adjusting current densities. Figure 4(c) shows the progression of STDP from full (100%) to null (0%) synaptic modification, exemplifying Hebbian learning. The results suggest that the skyrmion chamber's weight incorporates the STDP model principles, where synaptic modification depends on the order and relative timing of pre- and post-synaptic spikes, highlighting the complex interplay of factors contributing to synaptic plasticity.

This location dependence arises from neuromodulators like dopamine and acetylcholine, which modulate synaptic plasticity.[34–38] The degree of synaptic strengthening and weakening varies along the dendrite.[39] This principle of STDP-related varying rates of synaptic weight updates is implemented using different current densities within W. Figure 4(c) illustrates these variations, categorizing STDP rates as strong, moderate, and weak, corresponding to distinct learning locations along the dendrite. For moderate weight, current densities of $I_{12} = 3.5 \times 10^{11}$ A/m^2 $(-\hat{y})$ for LTP and $I_{23} = 2.5 \times 10^{11}$ A/m^2 $(-\hat{y})$ for LTD were used. For weak weight, $I_{12} = 1.5 \times 10^{11}$ A/m^2 $(-\hat{y})$ for LTP and $I_{23} = 0.5 \times 10^{11}$ A/m^2 $(-\hat{y})$ for LTD were used.

STDP ranges from 0 to 100 ns, representing 0%–100% weight change for a strong rate and 7%–73% for a moderate rate. The weak rate is 0%–27% for LTP and 0%–20% for LTD. Lower skyrmion counts make matching LTP/LTD rates harder for weak updates. However, tunable weight change rates allow for the adjustment of learning behavior, showcasing skyrmion-STDP's versatility.

The design supports natural skyrmion motion for mimicking plasticity without VCMA gates, as shown in Fig. 5. Material interfacial engineering[40] increases the local perpendicular anisotropy, creating a lower $K_u = 7.38 \times 10^5$ J/m^3 in the constriction between chambers.

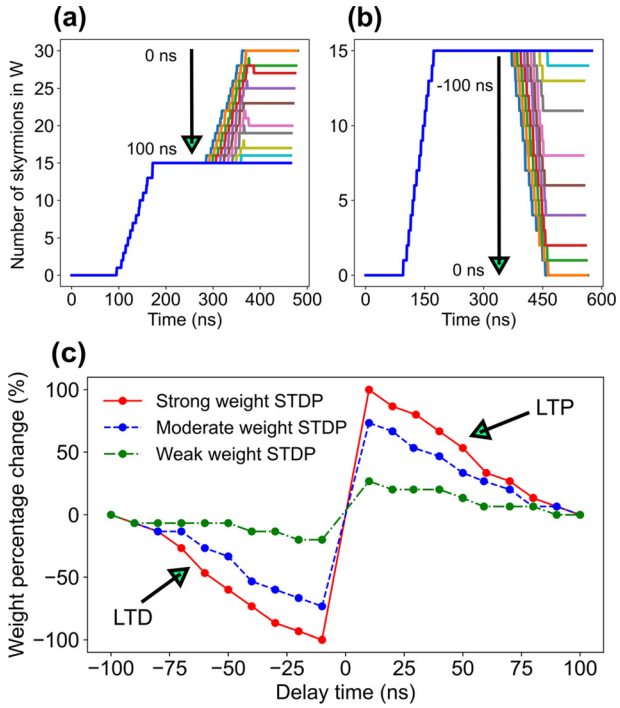

FIG. 4. STDP plasticity behavior and dendritic location-based plasticity rates. (a) LTP STDP: Skyrmion count in W over time for $\Delta t = 0$–100 ns. (b) LTD STDP: Skyrmion count in W for $\Delta t = -100$ to 0 ns. (c) Dendritic location-based STDP plasticity rates—strong (0%–100% weight change), moderate (7%–73%), and weak (0%–27% LTP, 0%–20% LTD).

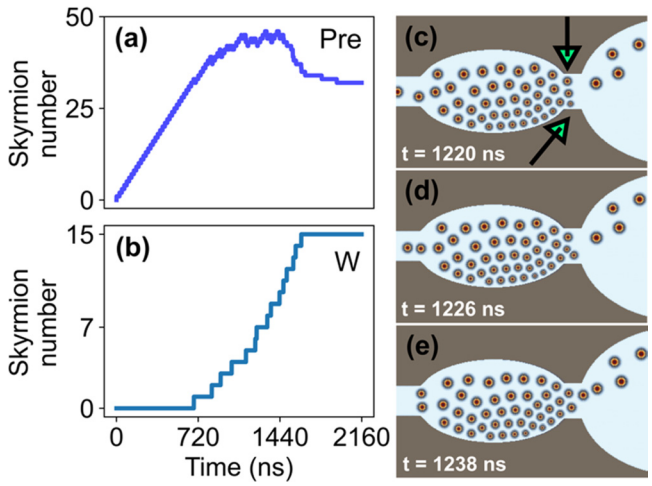

FIG. 5. Natural motion of skyrmions to mimic plasticity. (a) The weight at Pre shows the 32 skyrmion threshold for leakage to (b) W, and (c) shows a magnetization snapshot for skyrmions moving from Pre to W at t = 1220, (d) t = 1226, and (e) t = 1238 ns. Arrows show the forces applied to a skyrmion. Color represents M_z from −1 (red) to +1 (blue).

26 June 2024 14:52:50

Published under an exclusive license by AIP Publishing

Decreasing the current in Pre to $I_{12} = 1.2 \times 10^{11}$ A/m^2 $(-\hat{y})$ achieves natural motion. The Pre chamber holds fewer than 50 skyrmions [Fig. 5(a)], while the weight in W is shown in Fig. 5(b). The mechanism relies on repulsive forces between skyrmions moving through the constriction, as depicted by arrows in Fig. 5(c). It is worth noting that during the simulations, skyrmion annihilation events were observed, particularly at high current densities or when skyrmions were pushed against chamber edges during natural motion. However, for this study, the current density and geometry were optimized to minimize such events. The choice of elliptical chambers, as opposed to the circular chambers used in previous studies,[17,18,20] helped to improve skyrmion stability. As a result, skyrmion annihilation was relatively rare in the optimized device configuration and did not significantly impact the overall skyrmion count or device operation. Simulation snapshots [Figs. 5(c)–5(e)] illustrate these forces acting on a skyrmion. The decrease in skyrmion diameter signifies the skyrmion overpowering the constriction point energy barriers [Fig. 5(d)] and passing to the other side [Fig. 5(e)]. Details are visualized in the supplementary material video S2. Repulsive forces increase the total energy density within a skyrmion, enabling it to overcome the lowered anisotropy-induced energy barrier. Seventy skyrmions were introduced into Pre, and they move to W until the count reaches 32, beyond which the repulsive effect is insufficient for further movement. Current is only applied to I_{12} and I_{34}, while skyrmion–skyrmion repulsion causes expansion and movement inside W. Consequently, plasticity can be implemented using only two contact wires, simplifying the device design.

In summary, these results reveal that magnetic skyrmion chambers can be designed to emulate different types of synaptic plasticity, with STDP plasticity as an example. The chambers offer an adaptable architecture that enables the fine-tuning of STDP behavior by manipulating runtime, applied currents, and applied voltages. Key results include temporal- and diffusion-based control of skyrmion-synapse weight updates, STDP curves mimicking dendritic location-dependent plasticity, and nonvolatile synaptic weight storage. These results highlight the potential of skyrmion-based devices to achieve efficient, unsupervised learning in neuromorphic hardware. This biomimetic approach could lead to highly adaptable systems for real-world, online learning applications with further optimization and verification.

See the supplementary material for videos S1 and S2, which provide animated visualizations of the long-term potentiation process and the natural motion of skyrmions mimicking plasticity, respectively.

This work was supported by the National Science Foundation CAREER under Award No. 1940788. The authors acknowledge the Texas Advanced Computing Center (TACC) at The University of Texas at Austin for providing HPC resources that contributed to the research reported in this paper (http://www.tacc.utexas.edu).

AUTHOR DECLARATIONS

Conflict of Interest

The authors have no conflicts to disclose.

Author Contributions

Zulfidin Khodzhaev: Conceptualization (equal); Data curation (equal); Formal analysis (equal); Investigation (equal); Methodology (equal); Software (equal); Visualization (equal); Writing – original draft (equal); Writing – review & editing (equal). **Jean Anne C. Incorvia:** Conceptualization (equal); Data curation (equal); Funding acquisition (lead); Project administration (lead); Resources (lead); Supervision (lead); Writing – review & editing (equal).

DATA AVAILABILITY

The data that support the findings of this study are available within the article and its supplementary material.

REFERENCES

[1]A. Serb, J. Bill, A. Khiat, R. Berdan, R. Legenstein, and T. Prodromakis, "Unsupervised learning in probabilistic neural networks with multi-state metal-oxide memristive synapses," Nat. Commun. **7**(1), 12611 (2016).
[2]G. Milano, M. Luebben, Z. Ma, R. Dunin-Borkowski, L. Boarino, C. F. Pirri, R. Waser, C. Ricciardi, and I. Valov, "Self-limited single nanowire systems combining all-in-one memristive and neuromorphic functionalities," Nat. Commun. **9**(1), 5151 (2018).
[3]C. D. Schuman, T. E. Potok, R. M. Patton, J. D. Birdwell, M. E. Dean, G. S. Rose, and J. S. Plank, "A survey of neuromorphic computing and neural networks in hardware," arXiv:1705.06963 (2017).
[4]G. Indiveri, B. Linares-Barranco, T. J. Hamilton, A. van Schaik, R. Etienne-Cummings, T. Delbruck, S.-C. Liu, P. Dudek, P. Häfliger, S. Renaud, J. Schemmel, G. Cauwenberghs, J. Arthur, K. Hynna, F. Folowosele, S. Saïghi, T. Serrano-Gotarredona, J. Wijekoon, Y. Wang, and K. Boahen, "Neuromorphic silicon neuron circuits," Front. Neurosci. **5**, 73 (2011).
[5]M. Yao, O. Richter, G. Zhao, N. Qiao, Y. Xing, D. Wang, T. Hu, W. Fang, T. Demirci, M. De Marchi, L. Deng, T. Yan, C. Nielsen, S. Sheik, C. Wu, Y. Tian, B. Xu, and G. Li, "Spike-based dynamic computing with asynchronous sensing-computing neuromorphic chip," Nat. Commun. **15**(1), 4464 (2024).
[6]G. Q. Bi and M. M. Poo, "Synaptic modifications in cultured hippocampal neurons: dependence on spike timing, synaptic strength, and postsynaptic cell type," J. Neurosci. **18**(24), 10464–10472 (1998).
[7]A. Morrison, M. Diesmann, and W. Gerstner, "Phenomenological models of synaptic plasticity based on spike timing," Biol. Cybern. **98**(6), 459 (2008).
[8]R. C. Malenka and M. F. Bear, "LTP and LTD: An embarrassment of riches," Neuron **44**(1), 5–21 (2004).
[9]N. Caporale and Y. Dan, "Spike timing-dependent plasticity: A Hebbian learning rule," Annu. Rev. Neurosci. **31**, 25–46 (2008).
[10]R. C. Froemke and Y. Dan, "Spike-timing-dependent synaptic modification induced by natural spike trains," Nature **416**(6879), 433–438 (2002).
[11]P. Panda, J. M. Allred, S. Ramanathan, and K. Roy, "ASP: Learning to forget with adaptive synaptic plasticity in spiking neural networks," IEEE J. Emerging Sel. Top. Circuits Syst. **8**(1), 51–64 (2018).
[12]J. F. Hunzinger, V. H. Chan, and R. C. Froemke, "Learning complex temporal patterns with resource-dependent spike timing-dependent plasticity," J. Neurophysiol. **108**(2), 551 (2012).
[13]Z. Bing, I. Baumann, Z. Jiang, K. Huang, C. Cai, and A. Knoll, "Supervised learning in SNN via reward-modulated spike-timing-dependent plasticity for a target reaching vehicle," Front. Neurorobot. **13**, 18 (2019).
[14]P. A. Merolla, J. V. Arthur, R. Alvarez-Icaza, A. S. Cassidy, J. Sawada, F. Akopyan, B. L. Jackson, N. Imam, C. Guo, Y. Nakamura, B. Brezzo, I. Vo, S. K. Esser, R. Appuswamy, B. Taba, A. Amir, M. D. Flickner, W. P. Risk, R. Manohar, and D. S. Modha, "A million spiking-neuron integrated circuit with a scalable communication network and interface," Science **345**(6197), 668–673 (2014).
[15]M. Davies, N. Srinivasa, T.-H. Lin, G. Chinya, Y. Cao, S. H. Choday, G. Dimou, P. Joshi, N. Imam, S. Jain, Y. Liao, C.-K. Lin, A. Lines, R. Liu, D. Mathaikutty, S. McCoy, A. Paul, J. Tse, G. Venkataramanan, Y.-H. Weng, A. Wild, Y. Yang, and H. Wang, "Loihi: A neuromorphic manycore processor with on-chip learning," IEEE Micro **38**(1), 82–99 (2018).
[16]A. Fert, N. Reyren, and V. Cros, "Magnetic skyrmions: Advances in physics and potential applications," Nat. Rev. Mater. **2**(7), 17031 (2017).

26 June 2024 14:52:50

Published under an exclusive license by AIP Publishing

[17]J. Zázvorka, F. Jakobs, D. Heinze, N. Keil, S. Kromin, S. Jaiswal, K. Litzius, G. Jakob, P. Virnau, D. Pinna, K. Everschor-Sitte, L. Rózsa, A. Donges, U. Nowak, and M. Kläui, "Thermal skyrmion diffusion used in a reshuffler device," Nat. Nanotechnol. **14**(7), 658–661 (2019).
[18]D. Pinna, F. Abreu Araujo, J.-V. Kim, V. Cros, D. Querlioz, P. Bessiere, J. Droulez, and J. Grollier, "Skyrmion gas manipulation for probabilistic computing," Phys. Rev. Appl. **9**(6), 064018 (2018).
[19]K. M. Song, J.-S. Jeong, B. Pan, X. Zhang, J. Xia, S. Cha, T.-E. Park, K. Kim, S. Finizio, J. Raabe, J. Chang, Y. Zhou, W. Zhao, W. Kang, H. Ju, and S. Woo, "Skyrmion-based artificial synapses for neuromorphic computing," Nat. Electron. **3**(3), 148–155 (2020).
[20]Z. Khodzhaev, E. Turgut, and J. A. C. Incorvia, "Analysis of skyrmion shuffling chamber stochasticity for neuromorphic computing applications," IEEE Magn. Lett. **14**, 4500205 (2023).
[21]W. Jiang, X. Zhang, G. Yu, W. Zhang, X. Wang, M. Benjamin Jungfleisch, J. E. Pearson, X. Cheng, O. Heinonen, K. L. Wang, Y. Zhou, A. Hoffmann, and S. G. E. te Velthuis, "Direct observation of the skyrmion Hall effect," Nat. Phys. **13**(2), 162–169 (2017).
[22]X. Zhang, Y. Zhou, K. M. Song, T.-E. Park, J. Xia, M. Ezawa, X. Liu, W. Zhao, G. Zhao, and S. Woo, "Skyrmion-electronics: Writing, deleting, reading and processing magnetic skyrmions toward spintronic applications," J. Phys.: Condens. Matter **32**(14), 143001 (2020).
[23]E. Raimondo, E. Saugar, J. Barker, D. Rodrigues, A. Giordano, M. Carpentieri, W. Jiang, O. Chubykalo-Fesenko, R. Tomasello, and G. Finocchio, "Temperature-gradient-driven magnetic skyrmion motion," Phys. Rev. Appl. **18**(2), 024062 (2022).
[24]Y. Huang, W. Kang, X. Zhang, Y. Zhou, and W. Zhao, "Magnetic skyrmion-based synaptic devices," Nanotechnology **28**(8), 08LT02 (2017).
[25]S. Li, W. Kang, Y. Huang, X. Zhang, Y. Zhou, and W. Zhao, "Magnetic skyrmion-based artificial neuron device," Nanotechnology **28**(31), 31LT01 (2017).
[26]S. Qiu, J. Zeng, X. Han, and J. Liu, "On-chip skyrmion synapse regulated by Oersted field," AIP Adv. **14**(3), 035105 (2024).
[27]D. Das, Y. Cen, J. Wang, and X. Fong, "Bilayer-skyrmion-based design of neuron and synapse for spiking neural network," Phys. Rev. Appl. **19**(2), 024063 (2023).
[28]R. Legenstein, D. Pecevski, and W. Maass, "A learning theory for reward-modulated spike-timing-dependent plasticity with application to biofeedback," PLoS Comput. Biol. **4**(10), e1000180 (2008).
[29]S. Li, A. Du, Y. Wang, X. Wang, X. Zhang, H. Cheng, W. Cai, S. Lu, K. Cao, B. Pan, N. Lei, W. Kang, J. Liu, A. Fert, Z. Hou, and W. Zhao, "Experimental demonstration of skyrmionic magnetic tunnel junction at room temperature," Sci. Bull. **67**(7), 691–699 (2022).
[30]A. Vansteenkiste, J. Leliaert, M. Dvornik, M. Helsen, F. Garcia-Sanchez, and B. Van Waeyenberge, "The design and verification of MuMax3," AIP Adv. **4**(10), 107133 (2014).
[31]C. Moreau-Luchaire, C. Moutafis, N. Reyren, J. Sampaio, C. A. F. Vaz, N. V. Horne, K. Bouzehouane, K. Garcia, C. Deranlot, P. Warnicke, P. Wohlhüter, J. M. George, M. Weigand, J. Raabe, V. Cros, and A. Fert, "Additive interfacial chiral interaction in multilayers for stabilization of small individual skyrmions at room temperature," Nat. Nanotechnol. **11**(5), 444–448 (2016).
[32]P. Lai, G. P. Zhao, H. Tang, N. Ran, S. Q. Wu, J. Xia, X. Zhang, and Y. Zhou, "An improved racetrack structure for transporting a skyrmion," Sci. Rep. **7**(1), 45330 (2017).
[33]M. Ester, H.-P. Kriegel, J. Sander, and X. Xu, "A density-based algorithm for discovering clusters in large spatial databases with noise," in *Proceedings of the Second International Conference on Knowledge Discovery and Data Mining* (AAAI Press, 1996), pp. 226–231.
[34]J. C. Zhang, P. M. Lau, and G. Q. Bi, "Gain in sensitivity and loss in temporal contrast of STDP by dopaminergic modulation at hippocampal synapses," Proc. Natl. Acad. Sci. U. S. A. **106**(31), 13028–13033 (2009).
[35]L. Speranza, U. D. Porzio, D. Viggiano, A. de Donato, and F. Volpicelli, "Dopamine: The neuromodulator of long-term synaptic plasticity, reward and movement control," Cells. **10**(4), 735 (2021).
[36]H. Salgado, G. Köhr, and M. Trevīo, "Noradrenergic 'tone' determines dichotomous control of cortical spike-timing-dependent plasticity," Sci. Rep. **2**(1), 417 (2012).
[37]Z. Brzosko, W. Schultz, and O. Paulsen, "Retroactive modulation of spike timingdependent plasticity by dopamine," eLife **4**, e09685 (2015).
[38]S. Zannone, Z. Brzosko, O. Paulsen, and C. Clopath, "Acetylcholine-modulated plasticity in reward-driven navigation: A computational study," Sci. Rep. **8**(1), 9486 (2018).
[39]R. C. Froemke, M. M. Poo, and Y. Dan, "Spike-timing-dependent synaptic plasticity depends on dendritic location," Nature **434**(7030), 221–225 (2005).
[40]C. Denker, S. Nielsen, E. Lage, M. Römer-Stumm, H. Heyen, Y. Junk, J. Walowski, K. Waldorf, M. Münzenberg, and J. McCord, "Size and density control of skyrmions with picometer CoFeB thickness variations—Observation of zero-field skyrmions and skyrmion merging," J. Phys. D **56**(49), 495302 (2023).

26 June 2024 14:52:50

Published under an exclusive license by AIP Publishing